Physics and Imaging in Radiation Oncology 32 (2024) 100678

Contents lists available at ScienceDirect

Physics and Imaging in Radiation Oncology

journal homepage: www.sciencedirect.com/journal/physics-and-imaging-in-radiation-oncology

Original Research Article

Feasibility of quantitative relaxometry for prostate target localization and response assessment in magnetic resonance-guided online adaptive stereotactic body radiotherapy

Ergys Subashi [a,*], Eve LoCastro [b], Sarah Burleson [b], Aditya Apte [b], Michael Zelefsky [c], Neelam Tyagi [b]

[a] Department of Radiation Physics, University of Texas MD Anderson Cancer Center, Houston, TX, United States
[b] Department of Medical Physics, Memorial Sloan Kettering Cancer Center, New York, NY, United States
[c] Department of Radiation Oncology, New York University School of Medicine, New York, NY, United States

ARTICLE INFO

Keywords:
Quantitative MRI
Adaptive radiotherapy
MR-Linac

ABSTRACT

Purpose: Multiparametric magnetic resonance imaging (MRI) is known to provide predictors for malignancy and treatment outcome. The inclusion of these datasets in workflows for online adaptive planning remains under investigation. We demonstrate the feasibility of longitudinal relaxometry in online MR-guided adaptive stereotactic body radiotherapy (SBRT) to the prostate and dominant intra-prostatic lesion (DIL).

Methods: Fifty patients with intermediate-risk prostate cancer were included in the study. The clinical target volume (CTV) was defined as the prostate gland plus 1 cm of seminal vesicles. The gross tumor volume (GTV) was defined as the DIL identified on multiparametric MRI. Online adaptive radiotherapy was delivered in a 1.5 T MR-Linac using a prescription of 800 cGy/900 cGy × 5 fractions to the CTV + 3 mm/GTV + 2 mm. Relaxometry and diffusion-weighted imaging were implemented using clinically available sequences. Test-retest measurements were performed in eight patients, at each treatment fraction. Bias and uncertainty in relaxometry measurements were also assessed using a reference phantom.

Results: The bias in longitudinal/transverse relaxation times was negligible while uncertainty was within 3 %. Test-retest measurements demonstrate that bias/uncertainty in patient T1 and T2 were comparable to bias/uncertainty estimated in the phantom. Mean T1 and T2 relaxation were significantly different between the prostate and DIL. The correlation between T1, T2, and diffusion was significant in the DIL, but not in the prostate. During treatment, mean T1 in the DIL approaches mean T1 in the prostate.

Conclusions: Longitudinal relaxometry for online MR-guided adaptive SBRT is feasible in a high-field MR-Linac and may provide complementary information for target delineation and response assessment.

1. Introduction

The integrated MR-Linac provides a novel platform for offline, online, and real-time MR-guided adaptive radiotherapy (MRgART) [1–4]. The increased precision in target and organ-at-risk delineation has enabled treatment methods with ablative doses and improved outcomes [5–11]. The accuracy and efficiency of online MRgART will be further enhanced by automation techniques for segmentation [12], staging [13], and outcome modeling [14].

Anatomical imaging remains the most widely used modality for plan adaptation in MR-guided stereotactic body radiotherapy (SBRT). While functional, physiologic, and metabolic imaging features are known to be predictors of malignancy and treatment outcome [15–17], the inclusion of these datasets in workflows for online adaptive planning is in the validation phase and still under investigation. Recent work acknowledges spatiotemporal variations in tumor biology [18] and the importance of adaptation based on biologically-driven inputs [19]. Several groups have reported their initial experience with suitable measurement protocols for quantitative imaging and quality assurance trends in hybrid MR-Linacs [20–26].

Multiparametric MRI protocols have become one of the most important tools for detection, characterization, and categorization of

* Corresponding author at: Department of Radiation Physics, University of Texas MD Anderson Cancer Center, Houston, TX 77030, United States.
E-mail address: edsubashi@mdanderson.org (E. Subashi).

https://doi.org/10.1016/j.phro.2024.100678
Received 28 July 2024; Received in revised form 12 November 2024; Accepted 14 November 2024
Available online 16 November 2024

prostate lesions [27]. The longitudinal (T1) or transverse (T2) relaxation times and the apparent diffusion coefficient (ADC) have been shown to be significantly lower in prostate cancer when compared to non-cancerous tissue. These findings are valid at various magnetic field strengths and correlate with histology [28–43].

Online MR-guided adaptive SBRT to the prostate, with focal dose intensification to the dominant intraprostatic lesion (DIL), has recently been implemented in a high-field MR-Linac [10]. The aim of this work is to demonstrate the feasibility of longitudinal relaxometry measurements for online MRgART to the prostate and DIL. The leading hypothesis is that relaxometry will complement and may improve upon current clinical methods for target localization and response assessment.

2. Materials and methods

2.1. Adaptive treatment planning and delivery

Fifty consecutive patients with National Comprehensive Cancer Network (NCCN) defined intermediate-risk prostate cancer were included in this IRB approved study. Median (min–max) age was 70.5 (55–85) years old. Patients had one to four dominant intraprostatic lesions (DIL) identifiable on multiparametric MRI with a Prostate Imaging Reporting and Data System (PI-RADS) score of 3–5 [44]. To minimize the effect on longitudinal analysis, patients were excluded if relaxometry or diffusion measurements failed in two consecutive treatment fractions.

All patients were treated in an integrated 1.5 T MR-Linac (Elekta AB, Stockholm, Sweden). The clinical target volume (CTV) was defined as the prostate gland plus 1 cm of seminal vesicles at the base. The gross tumor volume (GTV) was defined as the DIL identified on multiparametric MRI during simulation in a 3.0 T scanner (Philips Healthcare, Best, the Netherlands) [45]. Prescription was 800 cGy × 5 to the CTV + 3 mm with an integrated boost of 900 cGy × 5 to the GTV + 2 mm, delivered every other day. Treatment planning was performed in the Monaco treatment planning system (Elekta AB, Stockholm, Sweden). Reference and daily online-adapted plans consisted of 15 IMRT beams spaced equidistantly while avoiding hardware in the cryostat pipe and couch. All plans were calculated using a 3.0 mm grid with a statistical uncertainty of 1.0 % per calculation. Delivery was in step-and-shoot mode using a dose rate of 425 MU/min at the isocenter. Daily contours for online plan adaptation were drawn on a 3D T2-weighted MRI scan (MRI_{plan}) using the following imaging parameters: TR/TE = 1300/87 ms, voxel size = 1 × 1 × 2 mm^3, FOV = 400 × 450 × 250 mm^3. Additional details for the workflow including simulation, planning, online adaptation, and delivery can be found in the literature [10]. Of note, all patients underwent placement of a hydrogel rectal spacer (SpaceOAR, Boston Scientific, Marlborough, MA, USA) approximately one week prior to simulation to increase the distance between the prostate gland and rectal wall.

2.2. Data acquisition

Relaxometry and diffusion-weighted imaging were implemented using clinically available sequences in the MR-Linac. T1 values were estimated with the variable flip-angle (VFA) method, T2 values were estimated with the multi-slice multi-echo (MSME) method, and the apparent diffusion coefficient was estimated with a multi b-value diffusion weighted acquisition. The implementation of these methods in the MR-Linac is described in detail elsewhere [26]. A brief summary for each technique and corresponding parameters is provided in Supplementary Materials.

The following imaging parameters were used in the measurement of T1 relaxation times: TR/TE = 20/2.3 ms, FA={4°, 22°}, number of excitations (NEX) = 1, acquisition matrix = 160x160, field of view = 320 × 320 mm^2, slice thickness = 3 mm, slice spacing = 1.5 mm, number of slices = 67 (axial), SENSE = 2 (RL, phase). Receiver gain settings were determined using FA = 15° and the same settings were used for both acquisitions in the VFA protocol. The total acquisition time per flip angle was ~ 45 s.

The following imaging parameters were used in the measurement of T2 relaxation times: TR/TE/ΔTE = 4000/22/11 ms, 8 echoes, NEX = 1, acquisition matrix = 160 × 160, field of view = 320 × 320 mm^2, slice thickness = 3 mm, slice spacing = 3 mm, number of slices = 33 (axial), SENSE = 2 (RL, phase). To minimize the effect of stimulated echoes, a dummy echo was generated and discarded before the echo-train used in the analysis. The total acquisition time was ~5.5 min.

Diffusion measurements were additionally performed in a subset of eight patients using a single-shot spin-echo EPI (SS-EPI) imaging sequence based on recommendations from the Unity MR-Linac consortium [21]. The following imaging parameters were used: b (NEX) = {0 (1), 10 (1), 40 (1), 70 (1), 90 (1), 100 (1), 120 (1), 170 (1), 210 (1), 240 (1), 270 (2), 390 (2), 500 (3), 620 (3) s/mm^2}, TR/TE = 6098/73 ms, acquisition matrix = 104 × 104 mm^2, field of view = 256 × 256 mm^2, slice thickness = 4 mm, number of slices = 30 (axial), SENSE = 2.5 (RL, phase), SPAIR fat suppression. The total acquisition time was ~6 mins.

The bias and uncertainty of relaxometry measurements were assessed using the phantom developed by the National Institute of Standards and Technology (NIST) and International Society of Magnetic Resonance in Medicine (ISMRM) [46]. This phantom includes two parallel plates containing vials with nominal relaxation rates. The phantom is positioned at the isocenter with the anterior coil placed flush on its surface. Room temperature was monitored and maintained in the range of 19–22 °C. The nominal relaxation rates were compared to the measured values with weekly scans over the course of eight weeks. The bias and uncertainty of ADC measurements are reported in literature [21,26,47].

Relaxometry test–retest measurements were performed in eight patients, at each treatment fraction. During online plan adaptation, relaxometry maps were acquired consecutively without changes in patient positioning. A schematic diagram of the acquisition timeline is shown in Supplementary Materials Fig S1.

2.3. Image analysis

For phantom measurements, the bias ($\mathscr{B}$) was defined as:

$$\mathscr{B} = \frac{\mathscr{D}_{Measured} - \mathscr{D}_{Nominal}}{\mathscr{D}_{Nominal}} \bullet 100\% \quad (1)$$

where $\mathscr{D}$ represents T1 or T2. Uncertainty was quantified using the percent coefficient of variation (COV):

$$COV = \frac{\sigma}{\mu} \bullet 100\% \quad (2)$$

where σ and μ represent the standard deviation and the mean value of the measured data. The analysis was performed in a circular ROI of 1-cm diameter centered on each vial of interest in the NIST/ISMRM phantom.

For each treatment fraction, all acquired patient images were imported in the computational environment for radiotherapy research (CERR) and automatically fused using rigid registration focusing within a region of 2.0 cm around the prostate [48]. The registrations were inspected by three board certified medical physicists and manual adjustments were made if needed. Contours were transferred to the relaxometry and diffusion-weighted datasets, and the mean values of T1/T2/ADC were extracted in the CTV and GTV. To remove the influence from the values within the GTV, the CTV contour did not include the contour of GTV (removed by Boolean operation). To minimize the bias from overlapping T1 and T2 values in the hydrogel, the spacer was manually contoured at each fraction for the first eight patients in the study. The mean T1 and T2 relaxation from the hydrogel spacer was

used to remove the values from the overlapping regions within the CTV and GTV by thresholding.

All statistical analysis was performed in MATLAB (MathWorks, Natick, MA, USA). Test-retest acquisitions were analyzed using Bland-Altman plots. For each patient, the mean value of T1 and T2 in the CTV and GTV was compared using the paired, two-tailed *t*-test. All correlations were evaluated using Spearman's rank correlation coefficient. Significance was determined based on a p-level less than 0.05.

3. Results

3.1. Longitudinal bias and uncertainty in NIST phantom

The feasibility of longitudinal relaxometry measurements was initially assessed using the NIST/ISMRM phantom. Fig. 1 presents the bias and uncertainty of measured T1 and T2 as compared to nominal and baseline values. The mean and standard deviation of measured values in Fig. 1 is from the combined data from eight weeks. Baseline values were calculated by averaging the measurements from the first four weeks of the study. Figure S2 in Supplementary Materials shows a representative example from the phantom measurements, and Figure S3 presents the longitudinal trend over eight weeks. When comparing to nominal phantom values, the range [min – max] of bias and COV for T1 were [−5.5 % – 0.9 %] and [1.7 % – 2.9 %], respectively; the range of bias and COV for T2 were [−2.9 % – 7.9 %] and [0.6 % – 1.5 %], respectively. When comparing to baseline values, the range of bias for T1 and T2 were [−1.3 % – −0.5 %] and [−0.2 % – 0.3 %], respectively. Baseline corrections do not affect the variance therefore the range for COV remains the same as when comparing with respect to nominal values. The correlation of bias and COV with mean T1 and T2 was not statistically significant ($p \gg 0.05$, for all cases), irrespective of whether the comparison was with nominal or baseline values.

3.2. Longitudinal relaxometry for online MRgART

Relaxometry measurements were successfully completed in 244/250 and 242/250 fractions for T1 and T2 mapping, respectively. None of the patients included in the study had failures in consecutive treatment fractions. The primary failure mode was inappropriate gain settings due to user error, which was addressed by increasing operator training. In our cohort of 50 patients, eight patients had two distinct DILs, one patient had three distinct DILs, and one patient had four distinct DILs within the prostate gland. Fig. 2 illustrates the potential use of relaxometry maps for target localization in online adaptive MR-guided planning. The contours for CTV and GTV were drawn on the 3D T2-weighted planning MRI scan, aided by the ADC map. In this example, the GTV can be clearly seen in the T2 map (arrows). An example where the GTV can be seen in the T1 map is shown in Supplementary Materials Fig. S4. Translations and rotations from the planning MRI to the T1 and T2 maps are plotted in Fig. 3. The translations and rotations (mean ± std.dev.) from the planning MRI to the T1 map were 0.1 ± 0.3 mm (Rt), 0.9 ± 0.2 mm (Post), 0.0 ± 0.4 mm (Inf), and 0.0 ± 0.1 deg (Roll), 0.0 ± 0.2 deg (Pitch), 0.0 ± 0.2 deg (Yaw), respectively. The translations and rotations from the planning MRI to the T2 map were 0.1 ± 0.3 mm (Rt), 1.9 ± 0.3 mm (Post), 0.8 ± 0.5 mm (Inf), and 0.1 ± 0.1 deg (Roll), 0.0 ± 0.1 deg (Pitch), 0.0 ± 0.2 deg (Yaw), respectively. The time (mean ± std.dev.) from the planning MRI to the T1 and T2 map was 11.8 ± 3.1 mins and 15.6 ± 3.3 mins, respectively.

The bias and uncertainty in test–retest acquisitions were estimated using the Bland-Altman plots shown in Fig. 4. The mean values of T1 and T2 in the CTV and GTV were not significantly different ($p \gg 0.05$, for all cases). The bias and limit of agreement (LoA = 2•σ) for T1 in the CTV and GTV were −0.5 %±4.6 % and −0.6 %±5.9 %, respectively. The bias and limit of agreement for T2 in the CTV and GTV were 0.3 %±2.7 % and −0.2 %±4.7 %, respectively. The volume of CTV and GTV as a function of fraction number is plotted in Supplementary Materials Fig. S5. The correlation of mean CTV or GTV volume versus fraction number was not significant ($p \gg 0.05$, for both cases).

The mean values of T1 and T2 relaxation in the CTV and GTV are compared in Fig. 5. When combining the data from all fractions, mean T1 and mean T2 in the GTV were significantly lower than in the CTV ($p \approx 10^{-5}$ for T1; $p \approx 10^{-25}$ for T2). T1 relaxation (mean ± std.dev.) in the GTV and CTV was 1484.4 ± 150.7 ms and 1525.8 ± 110.1 ms, respectively. T2 relaxation in the GTV and CTV was 107.6 ± 14.2 ms and 120.4 ± 12.1 ms, respectively. Mean T1 in the GTV was significantly correlated with fraction number ($p = 0.02$), approaching the mean value of T1 in the CTV. The correlation between mean T1 in the CTV or mean T2 in the CTV/GTV with respect to fraction number was not significant ($p \gg 0.05$, for all cases).

A comparison between T1 and T2 relaxation with ADC is shown in Fig. 6. In the GTV, we find that the correlation between mean ADC and mean T1 or T2 was significant ($p = 0.005$, both cases). The correlation coefficient for T1 vs ADC and T2 vs ADC in the GTV was $\rho = 0.45$ and $\rho = 0.46$, respectively. In the CTV, this correlation was not significant

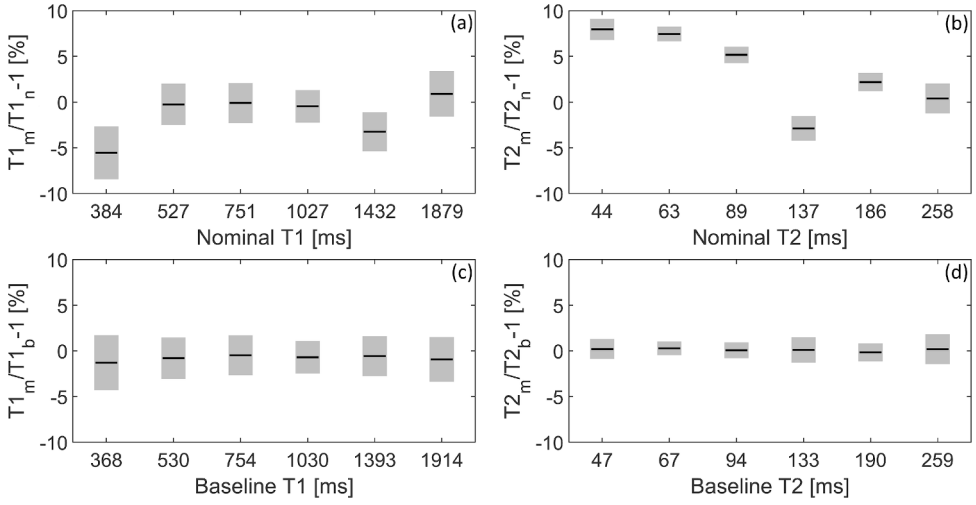

Fig. 1. Bias and uncertainty in relaxometry measurements in the NIST/ISMRM phantom. (a, b) The mean and standard deviation of measured T1 and T2 are compared with respect to the nominal phantom values. (c, d) The mean and standard deviation of measured T1 and T2 are compared with respect to the baseline values. Baseline values were calculated by averaging the measurements from the first four weeks of the longitudinal phantom study. (b = baseline, m = measured, n = nominal).

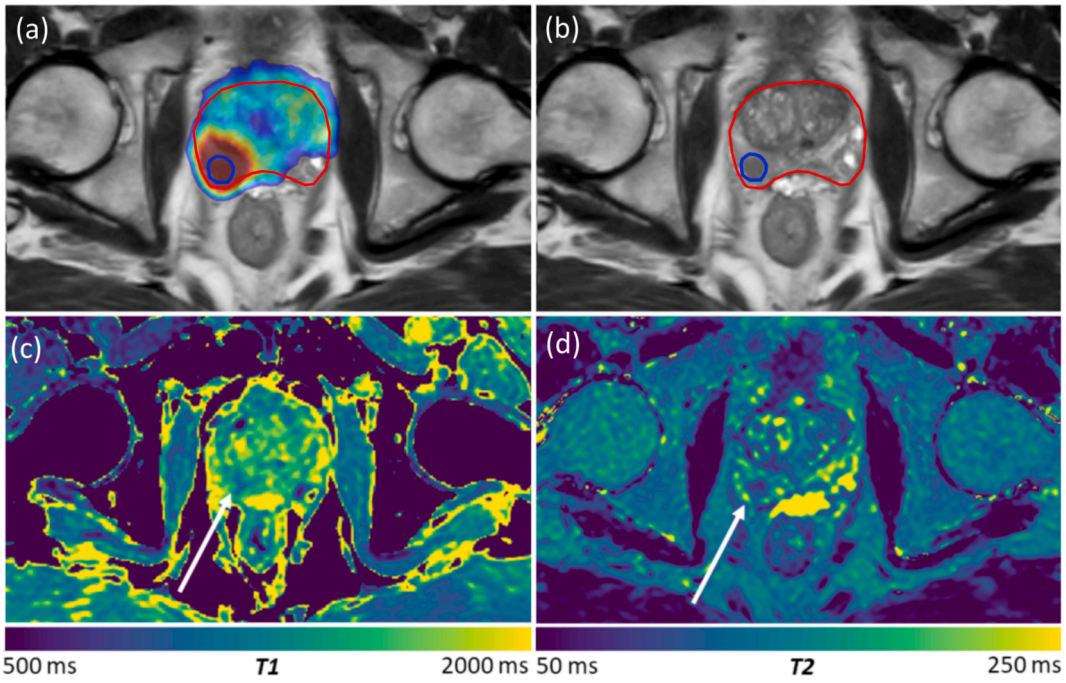

Fig. 2. Representative acquisitions from an online adaptive plan demonstrating (a) the dose distribution overlayed on T2-weighted MRI, (b) contours for the CTV and GTV, (c) T1-map, and (d) T2 map. Arrows in panels (c,d) point to the location of the GTV. The colormap for the dose distribution in panel (a) is in the range of the prescription, i.e. 800 cGy to 900 cGy.

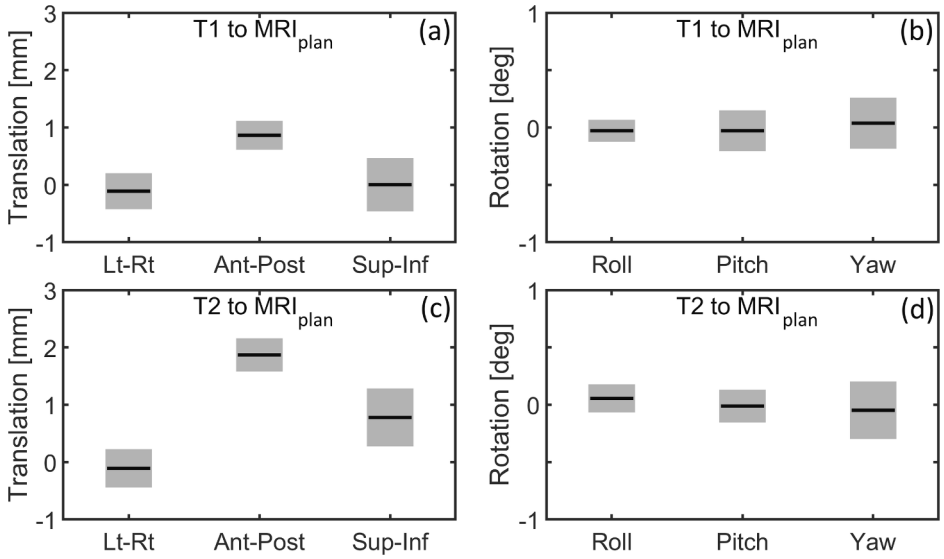

Fig. 3. Mean and standard deviation of translations and rotations from (a, b) planning MRI to T1 map and (c, d) planning MRI to T2 map. The time (mean ± std.dev.) from the planning MRI to the T1 and T2 map was 11.8 ± 3.1 mins and 15.6 ± 3.3 mins, respectively.

($p \gg 0.05$, both cases). The mean and standard deviation of the distribution of T1, T2, and ADC is compared in Supplementary Materials Fig. S6. In the subset of eight patients over five fractions, mean T1, T2, and ADC was significantly lower in the GTV when compared to the corresponding mean value in the CTV.

4. Discussion

The integrated MR-Linac provides a novel platform for precision radiotherapy. The availability of functional imaging biomarkers may enable further improvements by identifying high sensitivity and specificity features that can aid in target delineation and response assessment. In this work we demonstrate the feasibility of longitudinal relaxometry for online adaptive planning of prostate SBRT with focal dose intensification using a high-field MR-Linac.

The bias and uncertainty of T1 and T2 relaxation times, measured with clinically available MRI pulse sequences, were estimated in a NIST-traceable phantom and eight patients over five fractions. In phantom experiments, the mean bias with respect to nominal values for T1 and T2 was −1.5 % and 3.4 %, respectively. Previous work has also shown a consistently larger bias for nominal T2 values [20,26]. An example of the distribution of the excitation (B1) field measured in a uniform cylindrical phantom is given in Supplementary Materials Fig. S7. The average deviation of B1 with respect to nominal is 1.2 ± 0.2 %, with

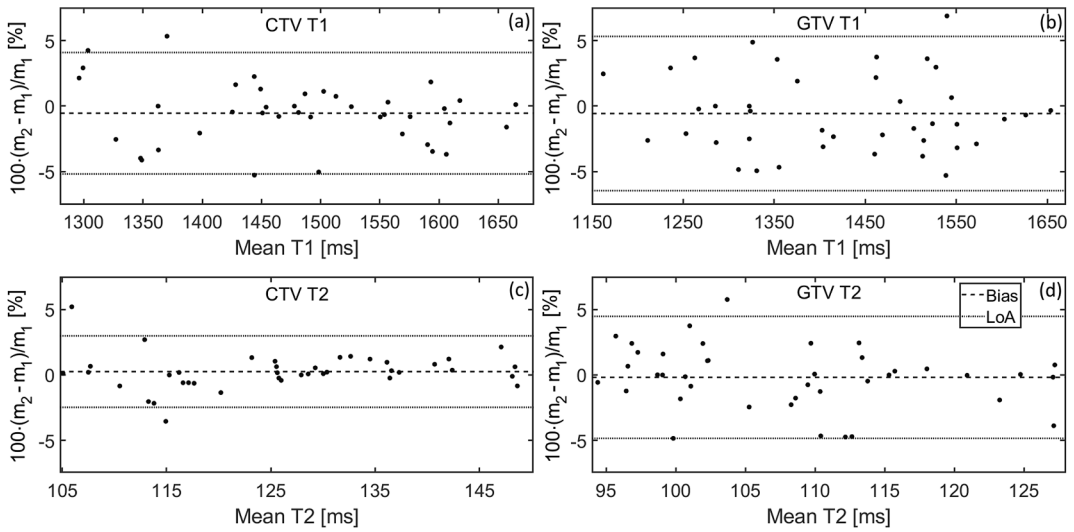

Fig. 4. Bland-Altman plots for test–retest acquisitions of relaxometry maps. (a, b) Comparison of mean T1 in CTV and GTV. (c, d) Comparison of mean T2 in CTV and GTV. The mean values of T1 and T2 were not significantly different between the two test–retest acquisitions. m1, m2 = first, second measurement.

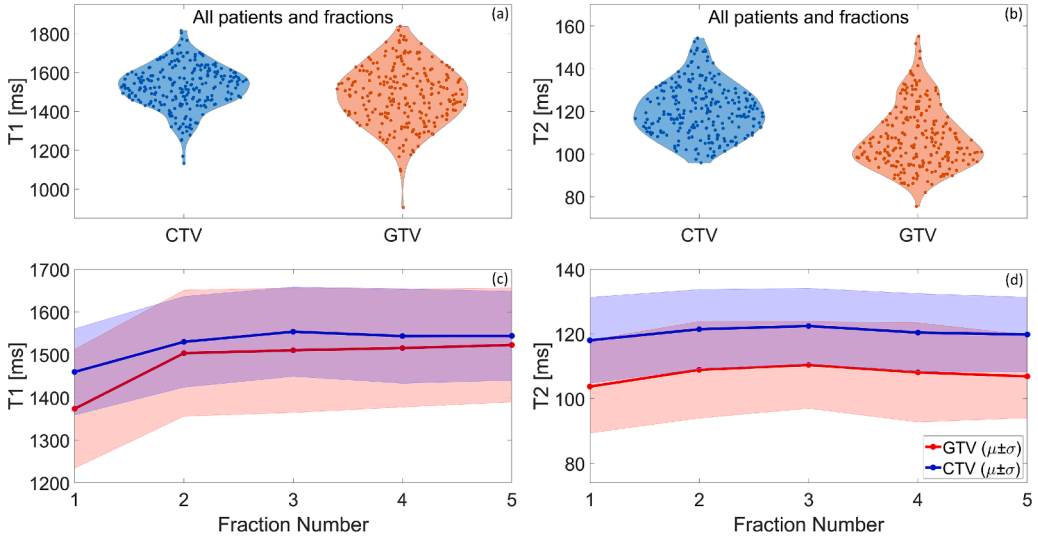

Fig. 5. Comparison of (a) mean T1 and (b) mean T2 values in the CTV and GTV. (c, d) Mean T1 and T2 in CTV and GTV as a function of fraction number. In the GTV, mean T1 and mean T2 was significantly lower than in the CTV. Mean T1 in the GTV was significantly correlated with fraction number ($p = 0.02$), approaching the mean value of T1 in the CTV. The correlation of mean T1 in the CTV and mean T2 in CTV or GTV with respect to fraction number was not significant.

minimal dependence on gantry position. When accounting for baseline differences, the mean bias for T1 and T2 was −0.8 % and 0.1 %, respectively. The mean COV for T1 and T2 was 2.2 % and 1.0 %. The uncertainty was not dependent on T1 or T2, as can be seen in Fig. 1 and Fig. 4. Note that for single-institutional studies, uncertainty may take priority over bias, particularly for biomarkers for which the biological interpretation is still under investigation. This is corroborated by our findings from the in vivo test–retest experiment where the mean bias for T1 and T2 was −0.5 % and 0.1 %. Furthermore, the uncertainty of T1 and T2 was comparable in phantom and patient measurements, with COV less than 3.0 % in both cases, indicating that it is feasible to achieve an average uncertainty that is primarily dictated by the MRI sequence parameters.

Mean T1 and T2 relaxation times are significantly lower in the dominant lesion and correlate significantly with ADC values, as shown in Fig. 5 and Fig. 6. On average, T1 and T2 in the GTV are approximately 3 % and 12 % lower than in the CTV. During the course of treatment, mean T1 relaxation in the GTV increased and approached the mean T1 relaxation in the CTV. While at baseline (fraction 1) the mean T1 is significantly lower in the GTV ($p = 0.0009$), at fraction 5 there is no significant difference between mean T1 in the GTV and CTV ($p = 0.2$). These findings suggest that relaxometry measurements may provide additional complementary information for online and offline plan adaptation, with T2 maps primarily enhancing target delineation and T1 maps assisting in treatment response assessment. It is worth stressing that our work demonstrates that current clinical methods provide sufficient sensitivity to measure changes in T1 that arise during the course of adaptive radiotherapy. However, our work does not show that T1 is measuring treatment response. While the correlation with diffusion provides insightful preliminary data for future work, further studies are needed to address the biological interpretation of T1 and T2 values. Note that hardware limitations may have a disproportionate influence on the accuracy of relaxometry and diffusion measurements, as shown in a representative patient with a hip implant in Supplementary Materials Fig. S8. The magnitude of system specific distortions has been estimated elsewhere [26]. The longitudinal analysis of diffusion weighted imaging

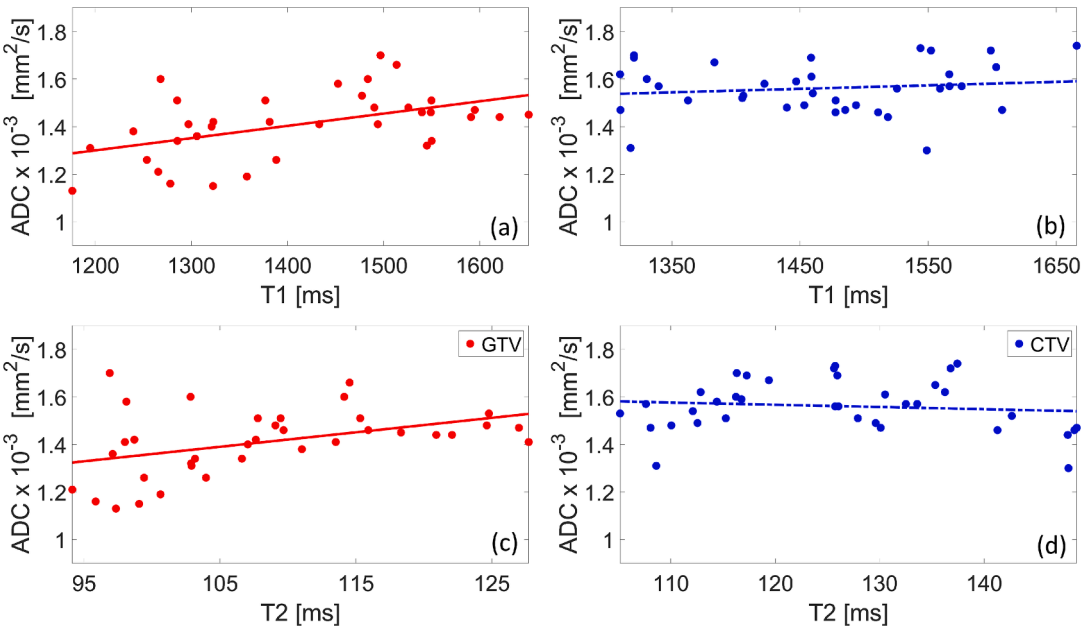

Fig. 6. Comparison of mean T1 and T2 with mean ADC in the (a, c) GTV and (b, d) CTV. The correlation between mean ADC and mean T1 or T2 in the GTV was significant ($p = 0.005$, both cases); the correlation was not significant in the CTV ($p \gg 0.05$, both cases).

for MR-guided online adaptive radiotherapy will be reported in future work.

In our study, intrafraction motion was assessed using rigid registration focused on a region around the prostate gland. Intrafraction translations were generally found to be small, with the worst case being on the order of the acquisition voxel size, as shown in Fig. 3 (refer to Fig. S9 in Supplementary Materials for translations and rotations in the test–retest study). While the use of rigid registration does not capture fine deformations due to changes in the surrounding anatomy, the use and validation of longitudinal deformable registration is still work in progress. Deformable registration will also help minimize the effects from the hydrogel spacer, which in our work was removed by thresholding (for hydrogel spacer: mean T1 = 2700 msec, mean T2 = 490 msec).

Multiparametric MRI protocols, particularly T2-weighted and diffusion weighted MRI, have become one of the most important tools available for detection, characterization, and categorization of prostate lesions. Morphologic and functional imaging features are known to be predictors of malignancy and treatment outcome [15–17]. Nevertheless, the inclusion of these protocols in workflows for online adaptive radiotherapy remains an open question.

The inclusion of functional, physiologic, and metabolic imaging in workflows for online adaptive radiotherapy remains under investigation, even though these datasets are known to be predictors of malignancy and treatment outcome. We demonstrate the feasibility of longitudinal relaxometry measurements for online MR-guided adaptive radiotherapy. Relaxometry maps provide measurements with minimal bias and sufficient precision to allow for differentiating between target subunits and for measuring changes during the course of therapy. The bias of T1 and T2 was negligible while the uncertainty, estimated by the COV, was less than 3 %. Test-retest measurements in eight patients over five fractions demonstrate that the bias and uncertainty of in vivo T1 and T2 were comparable to the bias and uncertainty of T1 and T2 in a NIST-traceable phantom. Mean T1 and T2 relaxation are significantly different between the prostate and DIL. The correlation between T1 and T2 with ADC is significant in the DIL, but not the prostate.

CRediT authorship contribution statement

Ergys Subashi: Conceptualization, Methodology, Investigation, Software, Writing – original draft. **Eve LoCastro:** Methodology, Writing – original draft, Software. **Sarah Burleson:** Methodology, Investigation, Writing – original draft. **Aditya Apte:** Methodology, Investigation, Supervision. **Michael Zelefsky:** Methodology, Investigation, Supervision. **Neelam Tyagi:** Conceptualization, Methodology, Investigation, Writing – original draft, Supervision.

Funding

This research was partially supported by the NIH/NCI Cancer Center Support Grant/Core Grant (P30 CA008748).

Declaration of competing interest

The authors declare that they have no known competing financial interests or personal relationships that could have appeared to influence the work reported in this paper.

Acknowledgements

The authors are grateful for the guidance and mentorship from Dr. Amita Shukla Dave.

Appendix A. Supplementary material

Supplementary data to this article can be found online at https://doi.org/10.1016/j.phro.2024.100678.

References

[1] Lagendijk JJW, Raaymakers BW, van Vulpen M. The magnetic resonance imaging-linac system. Semin Radiat Oncol 2014;24(3):207–9. https://doi.org/10.1016/j.semradonc.2014.02.009.

[2] Mutic S, Dempsey JF. The ViewRay system: magnetic resonance–guided and controlled radiotherapy. Semin Radiat Oncol 2014;24(3):196–9. https://doi.org/10.1016/j.semradonc.2014.02.008.

[3] Keall PJ, Barton M, Crozier S. The Australian magnetic resonance imaging–linac program. Semin Radiat Oncol 2014;24(3):203–6. https://doi.org/10.1016/j.semradonc.2014.02.015.

[4] Fallone BG. The rotating biplanar linac–magnetic resonance imaging system. Semin Radiat Oncol 2014;24(3):200–2. https://doi.org/10.1016/j.semradonc.2014.02.011.

[5] Reyngold M, Parikh P, Crane CH. Ablative radiation therapy for locally advanced pancreatic cancer: techniques and results. Rad Oncology 2019;14(1):95. https://doi.org/10.1186/s13014-019-1309-x.

[6] Henke L, Kashani R, Robinson C, Curcuru A, DeWees T, Bradley J, et al. Phase I trial of stereotactic MR-guided online adaptive radiation therapy (SMART) for the treatment of oligometastatic or unresectable primary malignancies of the abdomen. Radiother Oncol 2018;126(3):519–26. https://doi.org/10.1016/j.radonc.2017.11.032.

[7] Menten MJ, Wetscherek A, Fast MF. MRI-guided lung SBRT: Present and future developments. Phys Med 2017;44:139–49. https://doi.org/10.1016/j.ejmp.2017.02.003.

[8] Pathmanathan AU, van As NJ, Kerkmeijer LGW, Christodouleas J, Lawton CAF, Vesprini D, et al. Magnetic resonance imaging-guided adaptive radiation therapy: A "Game Changer" for prostate treatment? Int J Radiat Oncol Biol Phys 2018;100(2):361–73. https://doi.org/10.1016/j.ijrobp.2017.10.020.

[9] Tyagi N, Liang J, Burleson S, Subashi E, Godoy Scripes P, Tringale KR, et al. Feasibility of ablative stereotactic body radiation therapy of pancreas cancer patients on a 1.5 Tesla magnetic resonance-linac system using abdominal compression. Phys Imag Radiat Oncol. 2021;19:53-Epub 2021/07/27. doi: 10.1016/j.phro.2021.07.006. PubMed PMID: 34307919; PubMed Central PMCID: PMCPMC8295846.

[10] Brennan VS, Burleson S, Kostrzewa C, Godoy Scripes P, Subashi E, Zhang Z, et al. SBRT focal dose intensification using an MR-Linac adaptive planning for intermediate-risk prostate cancer: An analysis of the dosimetric impact of intra-fractional organ changes. Radiother Oncol 2023;179:109441. https://doi.org/10.1016/j.radonc.2022.109441.

[11] Tringale KR, Tyagi N, Reyngold M, Romesser PB, Wu A, O'Reilly EM, et al. Stereotactic ablative radiation for pancreatic cancer on a 1.5 Telsa magnetic resonance-linac system. Phys Imag. Radiat Oncol 2022;24:88–94.

[12] Elguindi S, Zelefsky MJ, Jiang J, Veeraraghavan H, Deasy JO, Hunt MA, et al. Deep learning-based auto-segmentation of targets and organs-at-risk for magnetic resonance imaging only planning of prostate radiotherapy. Phys Imag Radiat Oncol. 2019;12:80-6. Epub 2020/05/02. doi: 10.1016/j.phro.2019.11.006. PubMed PMID: 32355894; PubMed Central PMCID: PMCPMC7192345.

[13] Fehr D, Veeraraghavan H, Wibmer A, Gondo T, Matsumoto K, Vargas HA, et al. Automatic classification of prostate cancer Gleason scores from multiparametric magnetic resonance images. PNAS. 2015;112(46):E6265-73. Epub 2015/11/19. doi: 10.1073/pnas.1505935112. PubMed PMID: 26578786; PubMed Central PMCID: PMCPMC4655555.

[14] Apte AP, Iyer A, Thor M, Pandya R, Haq R, Jiang J, et al. Library of deep-learning image segmentation and outcomes model-implementations. Phys Med. 2020;73:190-6. Epub 2020/05/07. doi: 10.1016/j.ejmp.2020.04.011. PubMed PMID: 32371142; PubMed Central PMCID: PMCPMC8474066.

[15] Gillies RJ, Anderson A, Gatenby R, Morse D. The biology underlying molecular imaging in oncology: from genome to anatome and back again. Clin radiol 2010;65(7):517–21.

[16] Lambin P, Rios-Velazquez E, Leijenaar R, Carvalho S, Van Stiphout RG, Granton P, et al. Radiomics: extracting more information from medical images using advanced feature analysis. Eur J Cancer 2012;48(4):441–6.

[17] Lambin P, van Stiphout RGPM, Starmans MHW, Rios-Velazquez E, Nalbantov G, Aerts HJWL, et al. Predicting outcomes in radiation oncology—multifactorial decision support systems. Nat Rev Clin Oncol 2013;10(1):27–40. https://doi.org/10.1038/nrclinonc.2012.196.

[18] van der Heide UA, Thorwarth D. Quantitative Imaging for Radiation Oncology. Int J Radiat Oncol Biol Phys. 2018;102(4):683-6. Epub 2018/06/19. doi: 10.1016/j.ijrobp.2018.06.012. PubMed PMID: 29913252.

[19] Glide-Hurst CK, Lee P, Yock AD, Olsen JR, Cao M, Siddiqui F, et al. Adaptive radiation therapy (ART) strategies and technical considerations: a state of the ART review from NRG oncology. Int J Radiat Oncol Biol Phys 2021;109(4):1054–75.

[20] Kooreman ES, van Houdt PJ, Nowee ME, van Pelt VWJ, Tijssen RHN, Paulson ES, et al. Feasibility and accuracy of quantitative imaging on a 1.5 T MR-linear accelerator. Radiother Oncol. 2019;133:156-62. Epub 2019/04/03. doi: 10.1016/j.radonc.2019.01.011. PubMed PMID: 30935572.

[21] Kooreman ES, van Houdt PJ, Keesman R, Pos FJ, van Pelt VWJ, Nowee ME, et al. ADC measurements on the Unity MR-linac – A recommendation on behalf of the Elekta Unity MR-linac consortium. Radiother Oncol 2020;153:106–13. https://doi.org/10.1016/j.radonc.2020.09.046.

[22] Bruijnen T, van der Heide O, Intven MPW, Mook S, Lagendijk JJW, van den Berg CAT, et al. Technical feasibility of magnetic resonance fingerprinting on a 1.5T MRI-linac. Phys Med Biol. 2020;65(22):22nt01. Epub 2020/09/26. doi: 10.1088/1361-6560/abbb9d. PubMed PMID: 32977318.

[23] Chan RW, Lawrence LS, Oglesby RT, Chen H, Stewart J, Theriault A, et al. Chemical exchange saturation transfer MRI in central nervous system tumours on a 1.5 T MR-Linac. Radiother Oncol 2021;162:140–9.

[24] Mickevicius NJ, Kim JP, Zhao J, Morris ZS, Hurst Jr NJ, Glide-Hurst CK. Toward magnetic resonance fingerprinting for low-field MR-guided radiation therapy. Med Phys 2021;48(11):6930–40.

[25] Lewis B, Guta A, Mackey S, Gach HM, Mutic S, Green O, et al. Evaluation of diffusion-weighted MRI and geometric distortion on a 0.35 T MR-LINAC at multiple gantry angles. J Appl Clin Med Phys 2021;22(2):118–25.

[26] Subashi E, Dresner A, Tyagi N. Longitudinal assessment of quality assurance measurements in a 1.5 T MR-linac: Part II-Magnetic resonance imaging. J Appl Clin Med Phys. 2022;23(6):e13586. Epub 2022/03/doi: 10.1002/acm2.13586. PubMed PMID: 35332990; PubMed Central PMCID: PMCPMC9398228.

[27] Barentsz JO, Weinreb JC, Verma S, Thoeny HC, Tempany CM, Shtern F, et al. Synopsis of the PI-RADS v2 Guidelines for Multiparametric Prostate Magnetic Resonance Imaging and Recommendations for Use. Eur Urol. 2016;69(1):41-9. Epub 2015/09/12. doi: 10.1016/j.eururo.2015.08.038. PubMed PMID: 26361169; PubMed Central PMCID: PMCPMC6364687.

[28] Dregely I, Margolis DA, Sung K, Zhou Z, Rangwala N, Raman SS, et al. Rapid quantitative T(2) mapping of the prostate using three-dimensional dual echo steady state MRI at 3T. Mag Reson Med. 2016;76(6):1720-9. Epub 2016/01/15. doi: 10.1002/mrm.26053. PubMed PMID: 26765746.

[29] Foltz WD, Chopra S, Chung P, Bayley A, Catton C, Jaffray D, et al. Clinical prostate T2 quantification using magnetization-prepared spiral imaging. Mag Reson Med. 2010;64(4):1155-61. Epub 2010/06/22. doi: 10.1002/mrm.22492. PubMed PMID: 20564590.

[30] Gibbs P, Liney GP, Pickles MD, Zelhof B, Rodrigues G, Turnbull LW. Correlation of ADC and T2 measurements with cell density in prostate cancer at 3.0 Tesla. Invest Radiol. 2009;44(9):572-6. Epub 2009/08/21. doi: 10.1097/RLI.0b013e3181b4c10e. PubMed PMID: 19692841.

[31] Gibbs P, Tozer DJ, Liney GP, Turnbull LW. Comparison of quantitative T2 mapping and diffusion-weighted imaging in the normal and pathologic prostate. Mag Reson Med. 2001;46(6):1054-8. Epub 2001/12/18. doi: 10.1002/mrm.1298. PubMed PMID: 11746568.

[32] Giganti F, Gambarota G, Moore CM, Robertson NL, McCartan N, Jameson C, et al. Prostate cancer detection using quantitative T2 and T2-weighted imaging: The effects of 5-alpha-reductase inhibitors in men on active surveillance. J Magn Reson Imaging 2018;47(6):1646–53. https://doi.org/10.1002/jmri.25891.

[33] Langer DL, Kwast THvd, Evans AJ, Plotkin A, Trachtenberg J, Wilson BC, et al. Prostate Tissue Composition and MR Measurements: Investigating the Relationships between ADC, T2, Ktrans, ve, and Corresponding Histologic Features. Radiology. 2010;255(2):485-94. doi: 10.1148/radiol.10091343. PubMed PMID: 20413761.

[34] Langer DL, van der Kwast TH, Evans AJ, Trachtenberg J, Wilson BC, Haider MA. Prostate cancer detection with multi-parametric MRI: Logistic regression analysis of quantitative T2, diffusion-weighted imaging, and dynamic contrast-enhanced MRI. J Magn Reson Imaging 2009;30(2):327–34. https://doi.org/10.1002/jmri.21824.

[35] Liu W, Turkbey B, Sénégas J, Remmele S, Xu S, Kruecker J, et al. Accelerated T2 mapping for characterization of prostate cancer. Mag Reson Med. 2011;65(5):1400-6. Epub 2011/03/12. doi: 10.1002/mrm.22874. PubMed PMID: 21394778; PubMed Central PMCID: PMCPMC3079019.

[36] Sabouri S, Chang SD, Savdie R, Zhang J, Jones EC, Goldenberg SL, et al. Luminal Water Imaging: A New MR Imaging T2 Mapping Technique for Prostate Cancer Diagnosis. Radiology. 2017;284(2):451-9. Epub 2017/04/11. doi: 10.1148/radiol.2017161687. PubMed PMID: 28394754; PubMed Central PMCID: PMCPMC5522021.

[37] Sabouri S, Fazli L, Chang SD, Savdie R, Jones EC, Goldenberg SL, et al. MR measurement of luminal water in prostate gland: Quantitative correlation between MRI and histology. Journal of magnetic resonance imaging : J Magn Reson Imaging. 2017;46(3):861-9. Epub 2017/01/29. doi: 10.1002/jmri.25624. PubMed PMID: 28130866; PubMed Central PMCID: PMCPMC5557632.

[38] Skorpil M, Brynolfsson P, Engström M. Motion corrected DWI with integrated T2-mapping for simultaneous estimation of ADC, T2-relaxation and perfusion in prostate cancer. Magn Reson Imaging. 2017;39:162-7. Epub 2017/03/14. doi: 10.1016/j.mri.2017.03.003. PubMed PMID: 28286063.

[39] van Houdt PJ, Agarwal HK, van Buuren LD, Heijmink S, Haack S, van der Poel HG, et al. Performance of a fast and high-resolution multi-echo spin-echo sequence for prostate T(2) mapping across multiple systems. Magn Reson Med. 2018;79(3):1586-94. Epub 2017/07/04. doi: 10.1002/mrm.26816. PubMed PMID: 28671331; PubMed Central PMCID: PMCPMC5752635.

[40] Yamauchi FI, Penzkofer T, Fedorov A, Fennessy FM, Chu R, Maier SE, et al. Prostate cancer discrimination in the peripheral zone with a reduced field-of-view T(2)-mapping MRI sequence. Magn Reson Imaging. 2015;33(5):525-30. Epub 2015/02/18. doi: 10.1016/j.mri.2015.02.006. PubMed PMID: 25687187; PubMed Central PMCID: PMCPMC4426240.

[41] Panda A, Obmann VC, Lo W-C, Margevicius S, Jiang Y, Schluchter M, et al. MR fingerprinting and ADC mapping for characterization of lesions in the transition zone of the prostate gland. Radiology 2019;292(3):685–94. https://doi.org/10.1148/radiol.2019181705. PubMed PMID: 31335285.

[42] Yu AC, Badve C, Ponsky LE, Pahwa S, Dastmalchian S, Rogers M, et al. Development of a combined MR fingerprinting and diffusion examination for prostate cancer. Radiology 2017;283(3):729–38. https://doi.org/10.1148/radiol.2017161599. PubMed PMID: 28187264.

[43] Panda A, O'Connor G, Lo WC, Jiang Y, Margevicius S, Schluchter M, et al. Targeted biopsy validation of peripheral zone prostate cancer characterization with magnetic resonance fingerprinting and diffusion mapping. Invest Radiol 2019;54(8):485–93. https://doi.org/10.1097/rli.0000000000000569. PubMed PMID: 00004424-201908000-00006.

[44] Weinreb JC, Barentsz JO, Choyke PL, Cornud F, Haider MA, Macura KJ, et al. PI-RADS prostate imaging–reporting and data system: 2015, version 2. Eur Urol 2016;69(1):16–40.

[45] Tyagi N, Zelefsky MJ, Wibmer A, Zakian K, Burleson S, Happersett L, et al. Clinical experience and workflow challenges with magnetic resonance-only radiation therapy simulation and planning for prostate cancer. Phys Imag Radiat Oncol 2020;16:43–9. https://doi.org/10.1016/j.phro.2020.09.009.

[46] Keenan KE, Stupic KF, Boss MA, Russek SE, Chenevert TL, Prasad PV, et al. Comparison of T1 measurement using ISMRM/NIST system phantom. Singapore: Proc Inte Soc Magn Reson Med; 2016.
[47] Lawrence LSP, Chan RW, Chen H, Keller B, Stewart J, Ruschin M, et al. Accuracy and precision of apparent diffusion coefficient measurements on a 1.5 T MR-Linac in central nervous system tumour patients. Radiother Oncol 2021;164:155–62. https://doi.org/10.1016/j.radonc.2021.09.020.
[48] Deasy JO, Blanco AI, Clark VH. CERR: a computational environment for radiotherapy research. Med Phys 2003;30(5):979–85.